UNIVERSITI
MALAYSIA
PERLIS

Meso-porous-like tungsten oxide structure: A study on some physical properties at different deposited temperatures

Farhan A. Mohamed[1], Azhar I. Hassan[1], Evan T. Salim[1,*]

[1]Laser Science and Technology Branch, University of Technology, 10066 Baghdad, Iraq

ABSTRACT

Polycrystalline tungsten oxide (WO_3) thin films were prepared using the spray pyrolysis method at various substrate temperatures (200, 250, 300, 350, and 400 °C) on the quartz substrate. The X-ray diffraction pattern showed polycrystalline films with a monoclinic structure. Analysis using field-emission scanning electron microscopy revealed a porous fibrous reticulate morphology. The EDs results reflected the formation of stoichiometric films with optimum stoichiometry at 350 °C substrate temperature. The transmittance spectra at the 300–1100 nm spectral range reached about 55% with a direct band gap of 3.3 eV. The optical constant was also estimated and analyzed, where optical conductivity was found to be about 5.4669 x10^{14} (Ω cm)$^{-1}$ while, 2.09 eV was the value of Urbach energy at 350 °C.

Keywords: Meso-porous; tungsten oxide; thin films; polycrystalline structure; nanostructure.

1. INTRODUCTION

Manipulating and manufacturing of the oxide-based core-shell heterostructures, as well as the formation of interfaces between transition metal oxides, have ushered in a new era of materials research in recent years. It allows the pooling of an extremely discrete collection of coinciding material that attributes with increasing levels of experimental control. Transition metal oxides are semiconducting materials with large band gaps that can be adjusted in heterostructures. Tuning the band gap allows for quick charge transportation and provides unique photonic features that lack the possibility of achievement with a single component or comparable arrangements [1, 2].

Owing to its potential uses in sensors, solar cells, photocatalysis, and electrochromic devices, transition-metal oxides have elicited research interest. ZnO, TiO2, SnO_2, MoO_3, and WO_3 are the most often used semiconductor metal oxides in optoelectronic devices [3-5]. Meanwhile, tungsten trioxide (WO_3) thin films are not frequently used in device applications despite their remarkable features, such as exceptional chemical stability, substoichiometric nature, strong optical property, high thermal stability, and tunable electrical characteristics [6].

This oxide also has a large band-gap energy domain (2.6–3.6 eV) and a high absorption coefficient, rendering it feasible for front-contact use in photovoltaic solar cells [7]. Various techniques have been used to prepare WO_3 thin films, including evaporation [8], thermal reactive evaporation [9], sputtering [10,11], electrodeposition [12,13], anodization [14], pulsed-laser deposition [15], chemical vapor deposition [16], and sol–gel deposition [17,18].

Spray pyrolysis is a method of pyrolysis in which a substance is heated. It is a versatile deposition method since it enables the utilizing low-cost precursor materials, good layer-stoichiometry control, and large-area coatings with cost effective equipment and low-energy usage. In spray pyrolysis, the deposition rate, thickness, and homogeneity of the films are determined by nucleation and crystal growth processes, which are principally influenced by the substrate temperature and precursor-solution concentration. The rate of solvent evaporation within the aerosol droplets is affected by the precursor type and carrier gas pressure. Increasing the surface tension leads to speed up the droplets [19].

Spray pyrolysis has been used to deposit n-type tungsten oxide (WO_3) polycrystalline thin layers, with ammonium tungstate ((NH_4)$2WO_4$) as a precursor in the present study. The chemical deposition of WO_3 was conducted at different substrate temperatures. Then, the crystalline properties, surface morphology, optical and electrical properties were investigated and analyzed.

2. MATERIAL AND METHODS

2.1 Preparation of thin films

WO_3 thin films were deposited on commercially available glass substrates that had been cleaned with distilled water prior to use. Pre deposition, the substrates were also immersed for 15 minutes in a solution of 5% HCl and 95% double distilled water, washed with double distilled water, then ultrasonically cleaned with double distilled water for 15 minutes. Ammonium tungstate, a precursor solution made from H_2WO_4 powder (Merck), was used to deposit WO_3 thin films. Tungstic acid was dissolved in ammonium hydroxide (NH_4OH) at 80 °C with 10 min of stirring until a pure resolution was produced, yielding ammonium tungstate (0.01 mM) [19]:

$$H_2WO_4 + 2NH_4OH \xrightarrow{80\,^{o}C} (NH4)2WO4 + 2H2O \qquad (1)$$

At 200, 250, 300, 350, and 400 °C, ammonium tungstate was sprayed over the warmed glass substrates to prepare WO_3 films. The solvent evaporation and thermal fractionation of ammonium tungstate along with a thermal gradient resulted in WO_3 created by the spray-deposition technique [19]:

$$(NH_4)_2 WO_4 \xrightarrow{\Delta} WO_3 + 2NH_3 \uparrow + H_2O \uparrow \qquad (2)$$

The WO_3 films were uniform, adherent to the substrates, and slightly yellowish. To obtain homogeneous films, the spray nozzle height rate of spray, the air pressure and glass substrate dimension were kept constant throughout the spraying process at 28.5 cm, 3 mL/min, 1.72 bar, and (2*2) cm^2 respectively.

2.2 Characterization techniques

XRD, field-emission scanning electron microscopy (FE-SEM), energy-dispersive X-ray spectroscopy, UV–visible spectrophotometry, and I–V characteristics were used to investigate the deposited films. XRD was performed with a CuKα (0.15418 nm) radiation source to evaluate the structural characteristics of the WO_3 composite thin film. For the surface morphology and composition of the samples produced, FE-SEM was used. The roughness of the coated films was measured by atomic force microscopy. Optical characterizations of the WO_3 composite films were conducted with a UV-visible spectrophotometer (SHIMADZU UV-1800). The electrical conduciveness of the films was determined with a Keithley source meter (model 2400).

3. RESULTS AND DISCUSSIONS

X-ray diffraction (XRD) patterns revealed that the tungsten trioxide film was coated onto heated glass substrates at different temperatures with a volume of 50 mL. The concentration was fixed at 0.01 M as shown in Figure 1; the phase development of WO_3 layers was investigated by XRD within the 20°–60° range. An XRD pattern with a monoclinic crystal structure revealed the polycrystalline nature of WO_3 sheets (JCPDS card No. 96-210-6383). The strongest peaks were detected for the (200), (202), and (420) planes at 2θ = 24.5552°, 34.5302°, and 56.1457°, respectively, corresponding to 350 °C and 400 °C substrate temperatures obtained films. Compared with the (200) plane, the highest diffraction intensity at 24.555° (Ts = 350 °C) was stronger than those of the other planes [11]. The chemical reaction between the precursors takes place at 400 °C Ts. This occurs during deposition in the gaseous phase and produces the creation of a thin coating that is less homogenous [19]. The predominant development direction was detected along the (200) plane which agree with previous work [21]. In the case of 300 °C, it can be observed that one weak peak at plane (200), related to a thermal energy drop at this temperature, due to decreased grain size.
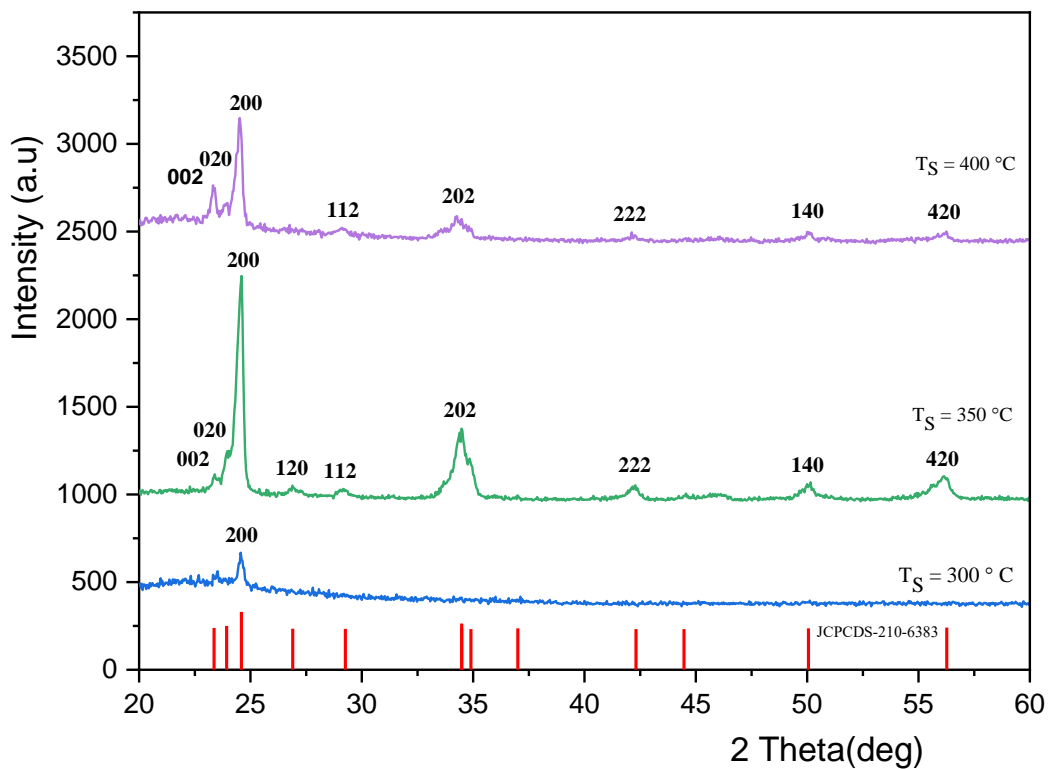
Figure 1. X-ray diffraction shapes of deposited WO_3 thin layer created utilising spray pyrolysis process at different substrate temperatures

The Debye–Scherrer eq. (3) was used to measure the average grain structure of the polycrystalline WO_3 films for the most intense peaks [22-25]:

$$D = \frac{0.9\lambda}{\beta \cos\theta} \tag{3}$$

In this equation, K is 0.9, λ is the wavelength (1.5418 Å), β is the full width at half-maximum of the diffraction peak, and θ is the diffraction angle.

The structural parameters [26-27], dislocation density (δ), and microstrain (ε) of the WO_3 thin-film coating were determined using eq. (4) and (5), and reported in Table 1:

$$\delta = \frac{1}{D^2} \tag{4}$$

$$\varepsilon = \frac{\beta \cos \theta}{4} \tag{5}$$

At substrate temperatures of 300 °C, 350 °C, and 400 °C, at triplet peak (002,020, and 200), the average crystallites' size (D) of WO_3 thin film were 21.5 nm, 23.11 nm, and 20.7 nm, respectively. The average values of (δ) and (ε) were (1.43 x 10 [14] lines m[-2], 2.04 x 10 [14] lines m[-2], and 2.59 x 10^{14} lines m[-2]) as well as (0.106 x 10 [-2] line m[-2], 0.154 x 10 [-2] line m[-2] and 0.173 x 10 [-2] line m[-2]). In addition, in metal oxides, there are numerous dangling bounds concerning the defects of metal and oxygen. Such defects were located at the boundaries of the grain. As a consequence, these defects are preferred in the merging process to produce bigger grains with an increase in the treatment temperature [29].

Table 1. WO_3 thin film structural properties at various substrate temperatures.

Ts (°C)	2θ(°)	hkl	d (Å)	FWHM (rad)	D (nm)	δ x 10[14] lines /m[-2]	ε x 10^{-3} line /m[-2]
300	23.494	002	3.78	0.00651	21.767	2.110	0.159
	23.9331	020	3.71	0.0000	0	0	0
	24.6037	200	3.61	0.00660	21.412	2.180	0.161
	23.49	002	3.78	0.00753	18.814	2.824	0.184
	23.93	020	3.71	0.00492	28.737	1.210	0.120
	24.55	200	3.62	0.00649	21.782	2.107	0.158
	26.95	120	3.30	0.00750	18.774	2.836	0.182
350	29.15	112	3.06	0.00854	16.396	3.719	0.206
	34.53	202	2.59	0.01336	10.348	9.338	0.319
	42.20	222	2.13	0.00858	15.742	4.035	0.200
	49.99	140	1.82	0.01026	12.783	6.118	0.232
	56.14	420	1.63	0.00865	14.769	4.584	0.190
400	23.37	002	3.80	0.00582	24.340	1.687	0.142
	23.93	020	3.71	0.00907	15.617	4.099	0.221
	24.52	200	3.62	0.00633	22.342	2.003	0.154
	29.12	112	3.06	0.01053	13.303	5.650	0.254
	34.35	202	2.60	0.01174	11.780	7.205	0.280
	42.16	222	2.14	0.00561	24.057	1.727	0.131
	50.05	140	1.82	0.00565	23.189	1.859	0.128

Figure 2 shows the FE-SEM images of spray-deposited WO$_3$ films on glass at different substrate temperatures (200–400 °C). The nanofibrous reticulated surface morphology were clearly visible [29]. This morphology was found all throughout the film surface. Additionally, for the similar film, a larger spatial-resolution FE-SEM image was generated. The network resembled that a fibrous bridge and the nanoporous surface morphology were demonstrated. The films appeared to be fibrous with multilayered structures at 200–300 °C, with distinct mean fiber widths of around 413, 462, and 450 nm and variable interspace lengths. The films were also very porous and had a consistent fibrous reticulated shape throughout the film at higher deposition temperatures [30, 31]. The film deposited at 250 °C for the same deposition period as that for the layer deposited at 300 °C was relatively porous. The morphologies of the layers were less porous and comprised several large particles buried in an amorphous matrix at lower deposition temperatures. The continuous semitransparent matrix appeared to be made up of huge droplets spreading out. This finding showed that particles descending on the substratum surface were still wet drops. Owing to the lower temperature of solvent evaporation, the arrived droplets were larger and heavier than those at higher deposition temperatures [32-34]. The porous fibrous structure grew at a larger fibre distance with a mean nanosize of 722.8 nm by increasing the temperature to 350 °C, whereas the interfiber distance of the cavities decreased to 204 nm [29]. Evidently, with temperature increased from 200 °C to 400 °C, the film shape changed from the highest density to the highest porosity. After compromise between porosity and adhesion, a layer deposited at Ts = 350 °C was selected for additional structure and electrical studies [35]. From the results of the FE-Scanning Electron Microscope, it was noticed that the thermal spraying technique strongly assisted to improve the structure and surface morphology of the tungsten oxide nanofibers.
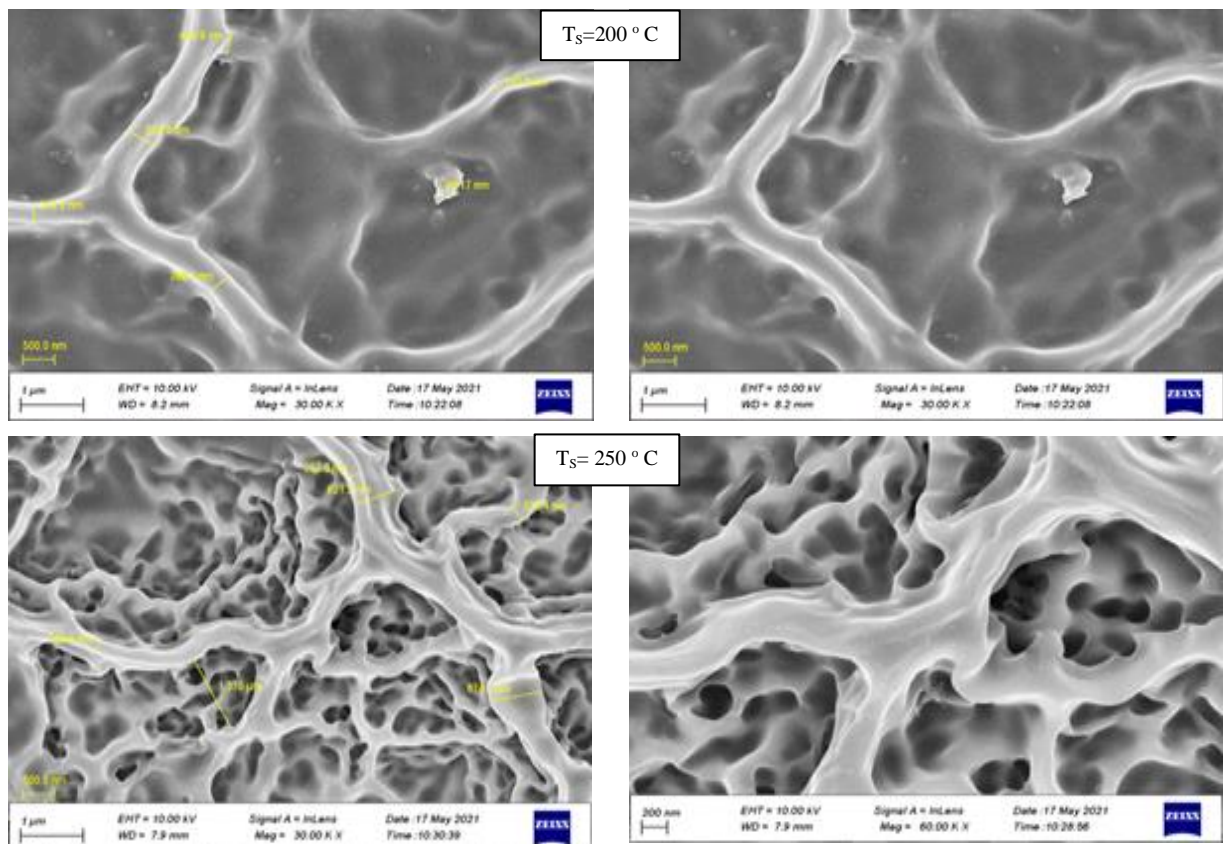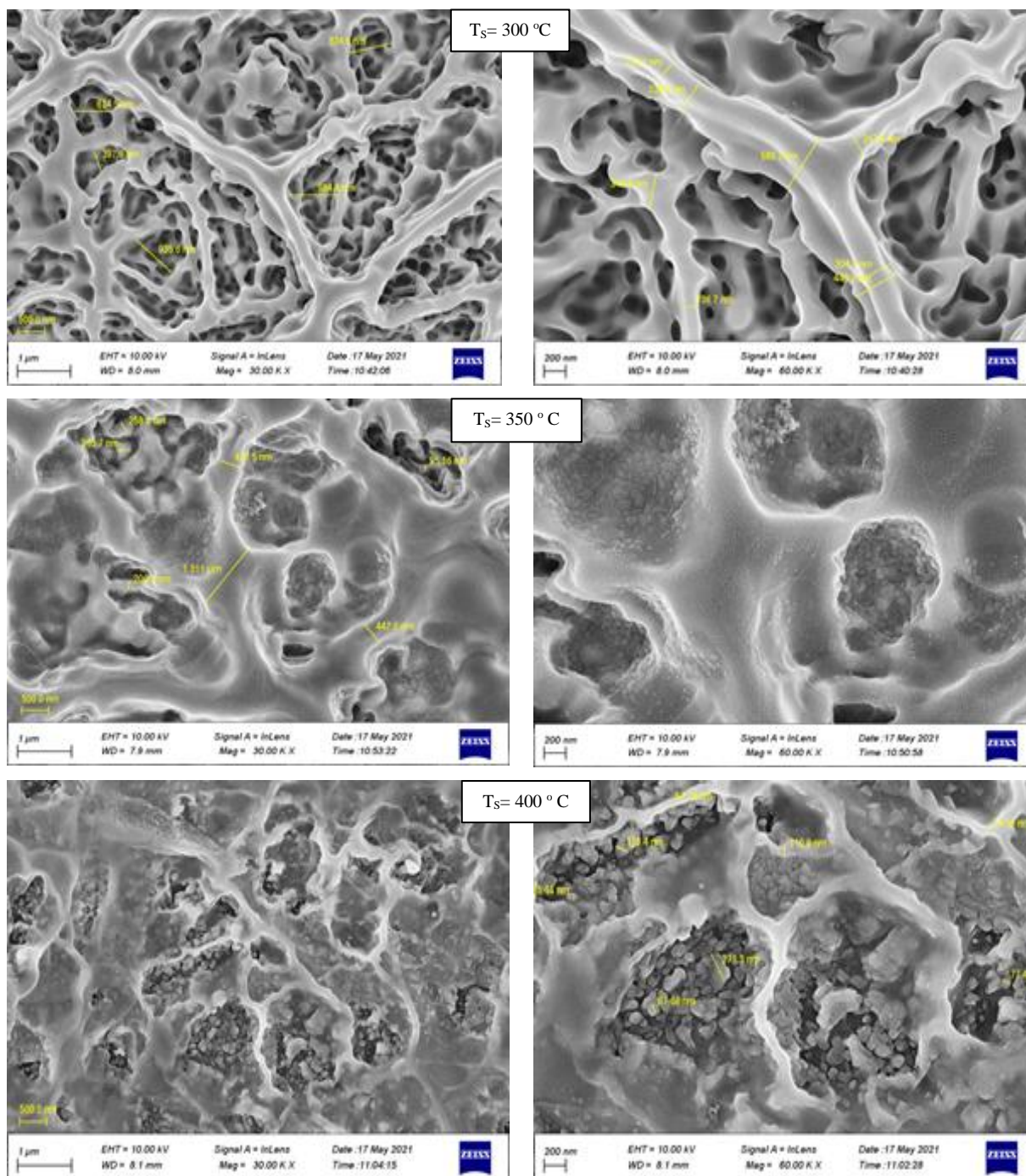
Figure 2. Filed Emission–Scan Electron Microscopy images of WO$_3$ thin films grown on various substrate temperatures

Figure 3 depicts the energy-dispersive spectra of WO$_3$ films grown at 200, 250, 350, and 400 °C on various substrates. The weight percentage of W content decreased at Ts (200–300 °C), whereas the weight percentage of O content increased. Owing to the partial dissociation, the oxygen level decreased with increasing the substrate temperature, reaching 26.72wt% in the films deposited at 350 °C. This finding meant that the films generated at high temperatures were substoichiometric WO3-y, with y being a minor percentage [36]. The FE SEM and the XRD patterns confirmed this conclusion. Evidently, the lack of oxygen in WO$_3$ layers boosted the electrical conductivity [36]. At Ts = 400 °C, the films contained 45.87wt% oxygen, suggesting that they reached their maximum oxidation state the Stoichiometry has been presented which refers to the

relationship between the quantities of reactants and products before, during, and following chemical reactions. [36], as presented in Table 2.
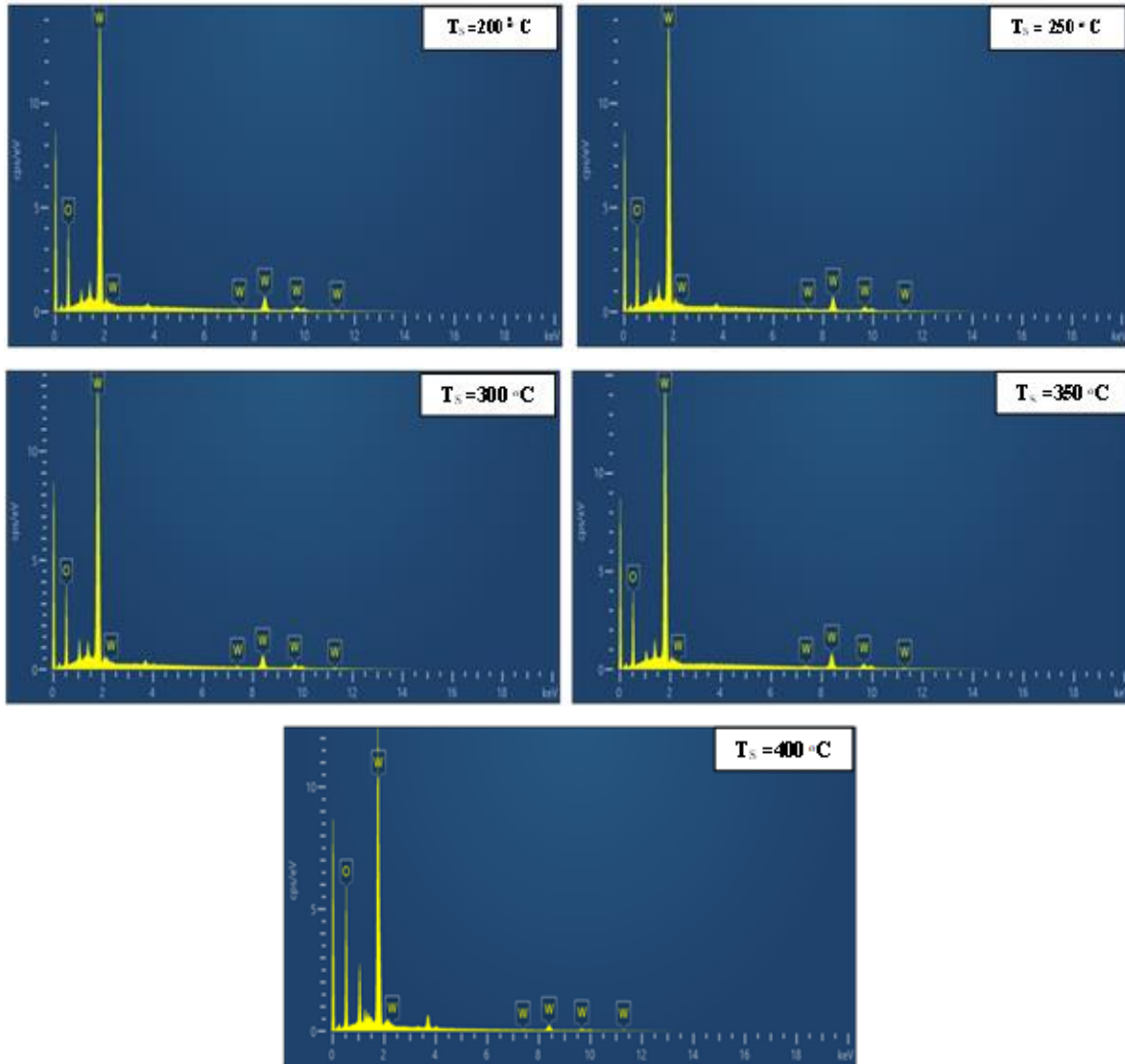
Figure 3. WO_3 layer EDS spectrum deposited at different temperatures

Table 2. Tungsten oxide thin film composition analysis(Stoichiometry) at different substrate temperatures

| Ts ($^\circ$C)	Weight percentage (Wt %)		W/O	Stoichiometry (%)
	W %	O %		
200	72.61	27.39	2.64	69.2
250	71.80	28.20	2.54	66.4
300	71.55	28.45	2.51	65.6
350	73.28	26.72	2.74	71.6
400	54.13	45.87	1.18	30.8
				30.8

The optical properties of WO$_3$ thin films were examined using UV-visible spectra within the wavelength range of 300–1100 nm. Variations in the transmission of tungsten oxide thin films at various deposition temperatures (200–400 °C) are displayed in Figure 4(a). Increasing the temperature of deposition led to an increased in the transmission [7]. The transmission of the tungsten oxide film prepared at Ts 300 °C is lower than that of the films prepared at Ts 350 and 400 ° C, indicating that the Wo$_3$ thin film lacks crystallinity and has a smaller crystalline size, causing it to absorb photons more in the visible range. At a substrate temperature of 400 °C, the film's T value was determined to be higher than the other films. As indicated in Table 2, this could imply that the thin layer is lacking in thickness and contains a significant amount of oxygen [38].

Uniform films were generated, droplets were poorly decomposed, and WO$_3$ films were transmitted at <350 °C by 30%, which was due to the generation of uneven films and insufficient breakdown of scraping droplets [26]. Additionally, the powdery layers that strongly dispersed the radiation of incidents at low substratum temperatures explained the limited transmission. The increase in tungsten oxide film transmission ranged within 350–400 °C was attributed to the decrease in layer thickness induced by the droplet spray that decreased with increased deposition temperature [26].

The absorbance spectra of WO$_3$ thin films formed at various substrate temperatures ranging from 300 nm to 1100 nm are shown in Figure 4(b). With increasing substrate temperature up to 300 °C, the WO3 thin-film absorption of light increased in the UV–visible region. The creation of oxygen vacancies in WO$_3$ sites may be the reason for this phenomenon [39]. The optical absorption of WO3 films decreased at 350–400 °C owing to the reduced layer thickness [40, 41]. The absorbance at 550 nm for films formed at 350 °C and 400 °C, respectively, was determined to be 0.8 and 0.3. Using optical-absorption measurements, the optical bandgap values of all samples were estimated. The absorption-spectrum values for semiconductors near band borders were investigated using the following classic relationship [30, 42, and 43]:

$$\alpha = \frac{\alpha_{O(h\upsilon - Eg)^n}}{h\upsilon} \tag{6}$$

where Eg represents the optical band gap energy between the bottom of the conduction band and the top of the valance band, hυ represents photon energy, and n represents a constant (1/2 for direct transition and 2 for indirect transition).
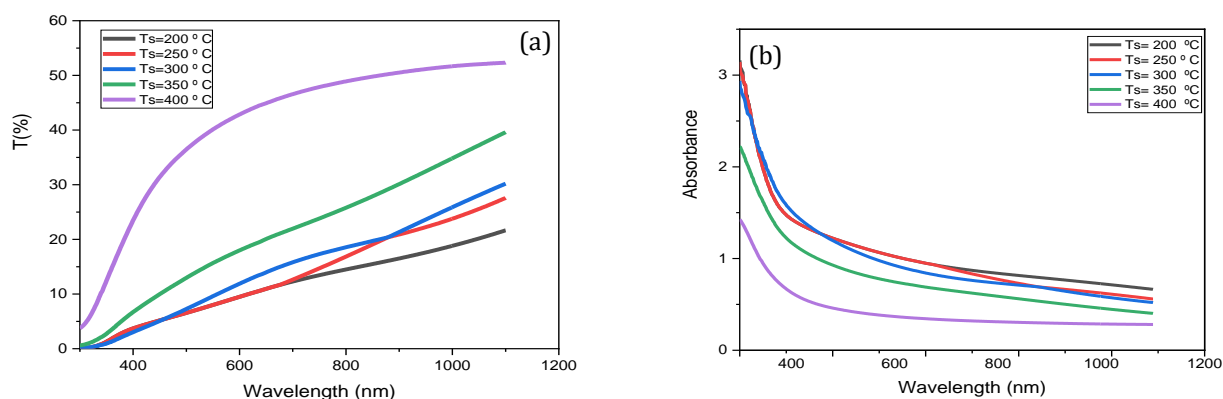
Figure 4. (a) WO$_3$ thin film spectra transmission and (b) absorbance at different temperatures on the substrate surface

For all WO_3 thin films, Figure 5 shows the change in $(\alpha h\upsilon)^2$ vs. $(h\upsilon)$. The plot's characteristics suggested the presence of a direct optical transition. The estimated energy gap (Eg) of the band was produced by projecting the right line to a coefficient of zero absorption. With increased substrate temperature to 350 °C, the optical Eg values of tungsten oxide decreased from 3.50 eV to 3.30 eV, might be related to increase in crystallinity of the thin films and in well agreement with XRD results and other published results [19, 22, 44]. Considering the creation of oxygen deficits around the Fermi level, a new deficiency was introduced. As a result of its proximity to the conduction band (CB), the surplus electrons arrived at the defect band's lower section, which was vacant [18, 39]. Oxygen deficit occurred in WO_3 at higher temperatures, so when the substrate was heated at 400 °C, the Eg values increased to 3.44 eV [11, 45].
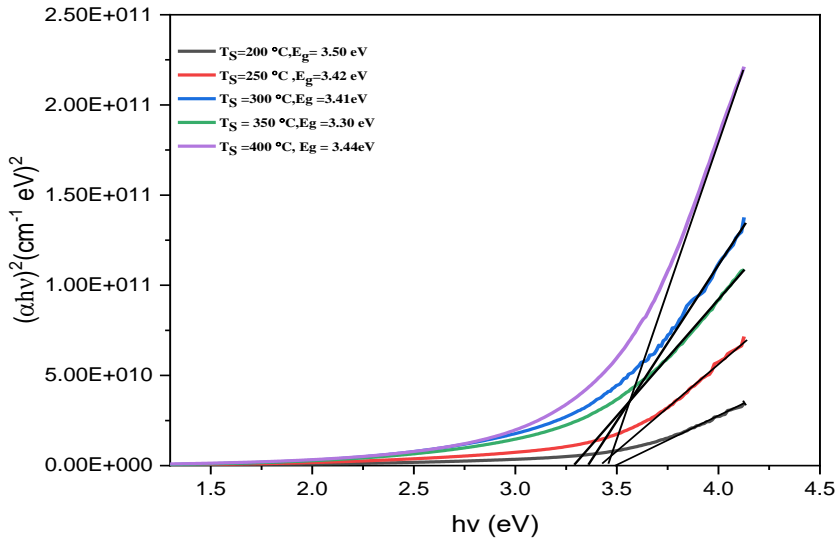
Figure 4. Plot of $(\alpha h\upsilon)^2$ vs. $h\upsilon$ for different Ts of WO_3 films

The coefficient of absorption varied exponentially with photon energy that was incident near the fundamental absorption edge and followed the well-known relationship with Urbach, which is represented as Eq. (7) [45-47]:

$$\alpha = \alpha_o \exp\left(\frac{h\upsilon}{E_U}\right) \tag{7}$$

where Eu is the energy of Urbach, which describes the breadth of the localized states in the bandgap, and α_o is a constant. In terms of absorption, the above equation can be expressed as follows [48, 49]:

$$A = A_O \left(\frac{h\upsilon}{E_U}\right) \tag{8}$$

The following relationships (Eqs. 9–11) were used to calculate the coefficient of absorption (α), coefficient of extinction (k), and optical conductivity (σ_{opt}) of tungsten oxide films [22, 50-52]:

$$\alpha = \frac{\ln\left(\frac{1}{T}\right)}{t} \tag{9}$$

$$K = \frac{\alpha\lambda}{4\pi} \tag{10}$$

$$\sigma_{opt} = \frac{nc\alpha}{4\pi} \tag{11}$$

where the transmittance, film thickness, wavelength, refractive index, and light velocity are represented by T, t, n, and c, respectively.

Table 3 presents the measured optical factors, k, Eg, σ_{opt}, and Eu. With increased substrate temperature to 350 °C, the estimated values of α, and k increased. The highest values were recorded at (α = 2.9912 x10^4 and k = 0.9335), then decreased at 400 °C. This finding was supported by previous research [37].

Table 3. The optical factors of WO$_3$ thin layers formed at changing   temperatures on glass substrates

Ts (°C)	Absorption coefficient x10^4 (α)	Extinction confficient (K)	Band gap (eV)	Optical conductivity $(\Omega$ cm$)^{-1}$	Urbach energy (eV)
200	1.3295	0.1936	3.50	6.9845 x1013	2.81
250	2.0124	0.7162	3.42	2.9872 x1014	2.63
300	2.3513	0.8257	3.41	4.1195 x1014	2.25
350	2.9912	0.9335	3.30	5.4669 x1014	2.09
400	1.2645	0.1791	3.44	1.9068 x1013	2.27

4. CONCLUSION

Polycrystalline WO$_3$ thin films could successfully prepared using spray pyrolysis method, where 350 °C was found to be the optimum substrate temperature, which revealed the formation of monoclinic crystal structure with main x-ray diffraction at the (200) diffraction plane. The diameter of the fibre was grown to 772.8 nm at 350 °C substrate temperature. According to the energy dispersal spectra of the formed tungsten oxide films at different temperatures of the substrate, it was discovered that the oxygen content was lowered and reached 26.72 per cent by weight in the films deposited at 350 °C. At 200–300 °C, the percentage of weight fell while the amount of O increased. The calculated Eg values reduced to 3.30 eV at the optimum temperature, according to the optical characteristics.

ACKNOWLEDGEMENTS

REFERENCES

[1]   Muhammad, A. I., Nitin, C., Online: vol 4 February (2017) pp. 1-11.

[2]   Vemuri, R. S., Bharathi, K. K., Gullapalli, S. K., and Ramana, C. V., ACS Appl. Mater. Interfaces, vil **2** issue 9 (2010) pp. 2623–2628.

[3]   Chang, M. T., Chou, L. J., Chueh, Y. L., Lee, Y. C., Hsieh, C. H., Chen, C. D., Chen, L., J. Nano-Mico Small, vol **3** issue 4 (2007) 658–664.

[4]   Akl, A. A., Kamal, H., & Abdel-Hady, K., Physica B: Condensed Matter, vol **325** (2003) pp. 65-75.

[5]   Youn, J. H., Baek, S. J., Kim, H. P. & Nam, D. H., Journal of Materials Chemistry C, vol **1** issue 19 (2013) pp. 3250–3254.

[6] Raja, M., Chandrasekaran, J., Balaji, M. & Kathirvel, P., Opt. - Int. J. Light Electron Opt., vol **145** (2017) pp. 169–180.

[7] Dabbous, S. & Nasrallah, T. Ben., Journal of Alloys and Compounds, vol **487** issue 1–2 (2009) pp. 286–292.

[8] Rao, M. C. Journal of Optoelectronics and Biomedical Materials, vol **3** issue 2 (2011) vol. 45–50.

[9] Porqueras, I. U. & Bertran, E., Thin Solid Films, vol **377–378** (200) pp. 8–13.

[10] Jin, C., Yamazaki, T., Shirai, Y. & Yoshizawa, T., Thin Solid Films, vol **474** issue 1–2 (2005) pp. 255–260.

[11] Simchi, H., Mccandless, B. E., Meng, T. & Shafarman, W. N., J. Alloys Compd., vol **617** (2014) pp. 609–615.

[12] Vijayalakshmi, R., Jayachandran, M. and Sanjeeviraja, C., Current Applied Physics, vol **3** issue 2–3 (2003) pp. 171–175.

[13] Krasnov, Y. S. & Kolbasov, G. Y., Electrochimica Acta, vol **49** issue 15 (2004) pp. 2425–2433.

[14] Di Paola, A. Di Quarto, and F. Sunseri, C. J. Electrochem. Soc., vol **125** issue 8 (1978) pp. 1344–1347.

[15] Tsoutsouva, M. G., Panagopoulos, C. N., Papadimitriou, D., Fasaki, I. & Kompitsas, M., Mater. Sci. Eng. B Solid-State Mater. Adv. Technol., vol. **176** issue 6 (2011) pp. 480–483.

[16] Ivanova, T., Gesheva, K. A., Popkirov, G., Ganchev, M. & Tzvetkova, E. Materials Science and Engineering B: Solid-State Materials for Advanced Technology, vol **119** issue 3 (2005) pp. 232-239.

[17] Deepa, M., Saxena, T. K., Singh, D. P., Sood, K. N. & Agnihotry, S. A., Electrochimica Acta, vol. **51** issue 10 (2006) pp. 1974-1989.

[18] Raja, M., Chandrasekaran, J. & Balaji, M. Materials Science in Semiconductor Processing, vol. **56** (2016) pp. 145–154.

[19] Bertus,L.M., and, Enesca, A. Thin Solid Films, vol **520** issue 13 (2012) pp. 4282–4290.

[20] Patil, P. R. & Patil, P. S.Thin Solid Films, vol. **382** issue 1–2 (2001) pp. 13–22.

[21] Dongale, T. D., Mohite, S. V, Bagade, A. A., Kamat, R. K. & Rajpure, K. Y. Microelectron. Eng., vol **183-184** (2017) pp. 12-18.

[22] Marnadu, R., Chandrasekaran, J., Maruthamuthu, S. & Balasubramani, V., Appl. Surf. Sci., vol **480** (2019) pp. 308–322.

[23] Dongale, T. D., Mohite, S. V., Bagade, A. A., Gaikwad, P. K. & Patil, P. S., Electron. Mater. Lett., vol **11** issue 6 (2015) pp. 944–948.

[24] Alsultany, F.H., Alhasan, S.F.H. & Salim, E.T., J Inorg Organomet Polym, vol **31** (2021) pp. 3749–3759.

[25] Abdul-Hamead, A. A., Othman, F. M. & Fakhri, M. A., Journal of Materials Science: Materials in Electronics, vol **32** (2021) pp. 15523–15532 .

[26] Shanmugasundaram, K., Thirunavukkarasu, P., Ramamurthy, M., Balaji, M. & Chandrasekaran, J. Orgenal Journal Chemistry, vol **33** issue 5 (2017) pp. 2484-2491.

[27] Fakhri, M. A., AbdulRazzaq, M. J., Alwahib, A. A. & Muttlak, W. H., Optical Materials, vol **109**. (2020) pp. 110363.

[28] Ismail, R. A., Salim, E. T. & Halbos, H. T. Optik, vol **245** (2021) pp. 167778.

[29] Bathe, S. R. & Patil, P. S. Solid State Ionics, vol **179** issue 9–10 (2008) pp. 314–323.

[30] Shendage, S. S., Patil, V. L., Patil, S. P., Vanalakar, S. A. & Bhosale, J. L., J. Anal. Appl. Pyrolysis, vol **125** (2017) pp. 9–16.

[31] Bathe, S. R. & Patil, P. S. Ã., Solar Energy Materials & Solar Cells, vol. **91** issue 12 (2007) pp. 1097–1101.

[32] Raj, M., Joseph, C., Subramanian, M., Perumalsamy, V., Elayappan, V., New J. Chem., vol. **44** issue 19 (2020) pp. 7708–7718.

[33] Fraga, L. E. & Zanoni, M. V. B. Journal of the Brazilian Chemical Society, vol **22** issue 4 (2011) pp. 718–725.

[34]   Schoonman, J. & Chen, C. J. Mater. Chem., vol **6** issue 5 (1996) pp. 765–771.

[35]   Matei, C., Landschoot, R. C. V., Thin Solid Films, vol **515** issue 13 (2007) pp. 5498-5504.

[36]   Rao, M. C. & Hussain, O. M., Research Journal of Chemical Sciences, vol **1** issue 7 (2011) pp. 92–95.

[37]   Marnadu, R., Chandrasekaran, J., Vivek, P., Balasubramani, V., Maruthamuthu, S., Zeitschrift fur Physikalische Chemie, vol **234** issue 2 (2019) pp. 355-379.

[38]   Mehnaz. S., Bhuiyan. A. H., Applied Physics A, vol **124** issue 57 (2018) pp. 1-11.

[39]   Rao, M. C.., Hussain O. M., Thin Solid Films, vol **1** issue 7 (2011) pp. 76–80.

[40]   Ganbavle, V. V., Kim, J. H. & Rajpure, K. Y. J. Electron. Mater., vol **44** issue 3 (2015) pp. 874–885.

[41]   Ganbavle, V. V, Agawane, G. L., Moholkar, A. V, Kim, J. H. & Rajpure, K. Y., Journal of Materials Engineering and Performance, vol **23** issue 4 (2014) pp. 1204-1213.

[42]   Salim, E. T., Ismail, R. A. & Halbos, H. T., Appl. Phys. A, **126** (2020) pp. 891.

[43]   Hassan, M. M. & Fakhri, M. A., Digest Journal of Nanomaterials and Biostructures., vol **14** issue 4 (2019) pp. 873-878.

[44]   Ganbavle, V. V, Mohite, S. V, Kim, J. H. & Rajpure, K. Y., J. Mater. Sci. Mater. Electron., vol **26** issue 8 (2015) pp. 6293–6305.

[45]   Liu, J., Zhang, G., Guo, K., Guo, D. & Shi, M., Micromachines, vol **11** issue 3 (2020) pp. 1-13.

[46]   Mukherjee, R. & Sahay, P. P., Electronic Materials Letters, vol **10** issue 2 (2014) pp. 401–410.

[47]   Taleb, S. M., Fakhri, M. A. & Adnan, S. A., Journal of Ovonic Research, vol **15** issue 4 (2019) pp. 261-269.

[48] Salim, E. T., Saimon, J. A., Abood, M. K. & Fakhri, M. A., Optical and Quantum Electronics, vol **52** issue 10 (2020) pp. 463.

[49] Badr, B. A., Mohammed, Q. Q., Numan, N. H., Fakhri, M. A. & Abdul Wahhab, A. W., International Journal of Nanoelectronics and Materials, vol **12** issue 3 (2019) pp. 283-290.

[50] Faisal, A. D., Ismail, R. A., Khalef, W. K. & Salim, E. T., Optical and Quantum Electronics, vol **52** (2020) pp. 1-12.

[51] Badr, B. A., Mohammed, Q. Q., Numan, N. H., Fakhri, M. A. & Abdul Wahhab, A. W., Journal of Ovonic Research, **15** issue 2 (2019) pp. 127-133.

[52] Fakhri, M. A., Abdulwahhab, A. W., Kadhim, S. M., Alwazni, M. S., & Adnan, S. A., Materials Research Express, vol **6** issue 2 (2018) pp. 026429.